© 2016. Published by The Company of Biologists Ltd | Journal of Cell Science (2016) 0, 1-10 doi:10.1242/jcs.179077

COMMENTARY

ARTICLE SERIES: IMAGING

# Three-dimensional visualisation of soft biological structures by X-ray computed micro-tomography

**Tom Shearer[1,2], Robert S. Bradley[3], L. Araida Hidalgo-Bastida[4], Michael J. Sherratt[5,*,‡] and Sarah H. Cartmell[1,*,‡]**


## ABSTRACT

Whereas the two-dimensional (2D) visualisation of biological samples is routine, three-dimensional (3D) imaging remains a time-consuming and relatively specialised pursuit. Current commonly adopted techniques for characterising the 3D structure of non-calcified tissues and biomaterials include optical and electron microscopy of serial sections and sectioned block faces, and the visualisation of intact samples by confocal microscopy or electron tomography. As an alternative to these approaches, X-ray computed micro-tomography (microCT) can both rapidly image the internal 3D structure of macroscopic volumes at sub-micron resolutions and visualise dynamic changes in living tissues at a microsecond scale. In this Commentary, we discuss the history and current capabilities of microCT. To that end, we present four case studies to illustrate the ability of microCT to visualise and quantify: (1) pressure-induced changes in the internal structure of unstained rat arteries, (2) the differential morphology of stained collagen fascicles in tendon and ligament, (3) the development of *Vanessa cardui* chrysalises, and (4) the distribution of cells within a tissue-engineering construct. Future developments in detector design and the use of synchrotron X-ray sources might enable real-time 3D imaging of dynamically remodelling biological samples.


**KEY WORDS: X-ray, Arteries, MicroCT, Tendon, Tissue engineering, Tomography**

## Introduction

In 1884, Edwin Abbott Abbott published his satire of English society ‘Flatland’, in which he imagined a two-dimensional (2D) world (Abbott, 2010). For most biologists, their ability to view microscopic biological structures and processes is similarly confined to two dimensions. Although several techniques for imaging the three-dimensional (3D) structure of biological samples are well-established, in practice they can be technically challenging, time-consuming, limited to small volumes and, in some cases, prone to inducing substantial structural artefacts. This Commentary critically appraises existing methods for visualising biological structures in 3D before discussing the historical development, current capabilities and future potential of X-ray computed micro-tomography (microCT) approaches for the rapid imaging of large volumes in dynamically remodelling biological systems. We illustrate the current capabilities of microCT through four case studies that focus, respectively, on: phase-contrast imaging, the use of X-ray contrast agents (stains), imaging a dynamic developmental process and cell labelling.

## Optical and electron microscopy in three dimensions

The desire to visualise the 3D micro-structure of biological samples is not new. For example, as early as 1914, Thyng obtained 3D reconstructions of human embryo from transverse histology sections (Thyng, 1914). However, despite recent technological advances in automated sectioning (Tapia et al., 2012) and high-resolution episcopic microscopy (Geyer et al., 2015), serial sectioning methods for visualising 3D structures within their physiological context remain a relatively specialised pursuit.

Sectioning methods are still used to reconstruct the 3D micro-morphology of, for example, rat brain (Schmitt et al., 2007) and collagen fibril alignment within tendons (Canty et al., 2006). Although the resulting sections can be readily stained to reveal compositional differences and fine structural detail when viewed by optical and transmission electron microscopy, respectively, these techniques remain laborious and prone to loss of data as a consequence of mechanical damage to fragile sections (Rastogi et al., 2013). Increasingly, serial block-face imaging is being adopted as a method of choice. In this technique, a mechanically robust specimen block (rather than delicate sections) might be visualised by either optical or scanning transmission electron microscopy. Although many sectioning artefacts are avoided using this approach, the technique remains relatively slow and, as yet, is not widely available (Weninger et al., 1998; Zankel et al., 2009). Alternatively, the internal structures of intact biological samples can also be visualised by confocal microscopy. This rapid and widely available technique can be combined with well-characterised chemical and immunological stains, or with complementary techniques, such as second-harmonic generation and auto-fluorescence, to visualise the 3D architecture of cells and extracellular matrix components, including fibrillar collagens and elastin (Cox et al., 2003; Navarro et al., 2004). Crucially though, the volume that can be visualised is usually limited by the opacity of the specimen and the resolution is not equivalent in all three dimensions. In Table 1, we compare optical and electron microscopy 3D visualisation methods according to their achievable resolution, imaging speed, potential to induce artefacts and availability (Weninger et al., 1998; O’Connell et al., 2005; Peddie and Collinson, 2014; Walton et al., 2015). We hope that this table will serve as an initial introduction to some of the more commonly adopted 3D visualisation techniques, but would

[1]School of Materials, University of Manchester, Manchester M13 9PL, UK. [2]School of Mathematics, University of Manchester, Manchester M13 9PL, UK. [3]Henry Moseley X-ray Imaging Facility, School of Materials, University of Manchester, Manchester M13 9PL, UK. [4]School of Healthcare Science, Manchester Metropolitan University, Manchester M15 6BH, UK. [5]Institute of Inflammation and Repair, University of Manchester, Manchester M13 9PL, UK.
*These authors contributed equally to this work

‡Authors for correspondence (michael.sherratt@manchester.ac.uk; sarah.cartmell@manchester.ac.uk)

T.S., 0000-0001-7536-5547; M.J.S., 0000-0003-4759-6617



**Received 14 October 2015; Accepted 24 March 2016**

Journal of Cell Science • Advance article



**JCS Advance Online Article. Posted on 8 June 2016**

Journal of Cell Science (2016) 0, 1-10 doi:10.1242/jcs.179077

**Table 1. Techniques for visualising the 3D structure of biological samples**

| | Visualisation method and specimen | | | |
|---|---|---|---|---|
| | **Optical or transmission electron microscopy of sequential sections** | **Optical or scanning electron microscopy of sequentially sectioned specimen block faces** | **Confocal microscopy of intact, semi-transparent, thin or small-volume specimens** | **X-ray tomography (laboratory and synchrotron sources) of intact, opaque and relatively large specimens** |
| **Specimen** | Physical sections | Block face (serially sectioned) | Intact (thin or small) | Intact |
| **Resolution ($x$, $y$, $z$)** | 1 µm, 1 µm, >10 µm (optical) <1 nm, <1 nm, >100 nm (electron) | 1 µm, 1 µm, >10 µm (optical) 1 nm,1 nm, >100 nm (electron) | 1 µm, 1 µm, >10 µm | Volume dependent (150 nm to >10 µm in $x$, $y$ and $z$) |
| **Specimen volume** | µm$^3$ | µm$^3$ | µm$^3$ | µm$^3$–cm$^3$ |
| **Speed** | Weeks or months | Days or weeks | Minutes | Seconds or minutes (synchrotron), hours (laboratory) |
| **Compositional information** | Conventional histological stains; immunological techniques | Conventional histological stains (optical); assumed from structure (electron) | Conventional histological stains; immunological techniques | Assumed from structure |
| **Potential sources of artefacts** | Sample preparation: dehydration, fixation, staining, sectioning induced holes and compressions, lost and damaged sections<br>Imaging: radiation damage (including shrinkage) | Sample preparation: dehydration, fixation, staining, sectioning induced knife marks and debris<br>Imaging: radiation damage (including shrinkage) | Sample preparation: dehydration, fixation, labelling (commonly with fluorescent probes and tags)<br>Imaging: photo-bleaching | Sample preparation: none (native tissues), dehydration and fixation (histological samples)<br>Imaging: radiation damage (oxidation and heating) |
| **Availability and cost** | Widely available, medium-high cost | Recently introduced, medium-high cost | Widely available, low cost | Recently introduced (laboratory); national facilities (synchrotron), medium-high cost |

encourage the interested reader to consult more specialised publications on specific approaches.

Although the techniques described above and in Table 1 are well-established, there are alternative emerging approaches that show promise, including optical projection tomography (OPT), a form of tomography based on optical microscopy. Although OPT is capable of achieving resolutions of the order of a few microns and has been used to visualise samples with a thickness up to 15 mm (Sharpe et al., 2002), it can only be applied to transparent samples (Geyer et al., 2015) and is, therefore, inappropriate for many soft tissues. Magnetic resonance microscopy (MRM or µMRI), however, can readily image opaque samples, such as chemically fixed mouse heart at micron-scale resolutions (Burton et al., 2014). A key advantage of MRM is the ability to conduct longitudinal imaging studies in living samples and, as a consequence, the technique has proven useful in characterising small animal models of disease (Yang et al., 2004) and in labelling viable cells with micron-sized iron oxide particles (Shapiro et al., 2004). The reader is referred to an excellent book chapter by Badea and Johnson for an in-depth discussion of the technique (Badea and Johnson, 2013). However, compared with OPT and MRM, microCT can readily resolve micron-scale features in opaque samples with dimensions measured in mm to cm. The remainder of this article thus concentrates on the application of X-ray tomography to biological samples.

## MicroCT then and now

X-ray radiographs, which were discovered by Wilhelm Conrad Röntgen in 1895 (Röntgen, 1895), were rapidly pressed into clinical use in just one year in order to detect bullets embedded in the tissues of wounded soldiers (Norton, 1896). However, it was not until the 1930s that the first attempts were made to image 3D structures with X-rays (X-ray tomography) (Craig, 1936). These early investigations eventually led to the introduction of hospital-based CT scanners in the 1970s and the subsequent award of the 1979 Nobel Prize for Physiology or Medicine to Allan Cormack and Godfrey Hounsfield. At the time of writing, in 2016, whole-body clinical CT scanners commonly achieve resolutions ranging from 1 mm to 250 µm, whereas higher resolution limb-extremity CT scanners can resolve features that measure 40 µm (Popp et al., 2012). In common with these clinical CT machines, laboratory-based microCT instruments construct 3D volumes by computationally processing a large number (hundreds or thousands) of 2D radiographs taken at sequential angles. The first laboratory microCT instruments, which were introduced in the early 1980s (Elliott et al., 1981; Elliott and Dover, 1982) and could achieve a spatial resolution of ∼10 µm, were typically used to image inorganic materials and the internal structures of fossils and calcified bones (Müller et al., 1994; Hildebrand and Rüegsegger, 1997; Rüegsegger et al., 1996). In the latter case, the availability of detailed 3D maps of the bone microstructure was quickly exploited to model the mechanical behaviour of these tissues (Hvid et al., 1989). These early successes led to the adoption of microCT by the biomedical engineering community to characterise the structure of calcified tissues, hydroxyapatite scaffolds and porous polyglycolic acid scaffolds (Müller et al., 1997; Folch et al., 2000; Cartmell et al., 2004, 2014). Importantly, the 3D volumes microCT generates can be segmented and interrogated to provide not only useful qualitative visual information but also quantitative measurements of, for example, the volume fraction of discrete components and their porosity and interconnectivity (Keyes et al., 2013; Nakayama et al., 2011). The principles by which these machines operate are relatively simple. In common with clinical CT scanners, microCT instruments employ an X-ray source and a detector but rotate the specimen. The internal architecture and operation of a typical instrument are described in Fig. 1.

Recently, there have been substantial advances in microCT technology, both in terms of the types of scanner available, which now allow sub-micron resolution, capture of phase-contrast information and faster scan acquisition, and in the development of imaging protocols (Withers, 2007; Stock, 2008; Bravin et al., 2013; Maire and Withers, 2014; Shearer et al., 2014; Balint et al., 2016). Collectively, these advances can be exploited to image soft (non-calcified) tissues. In the following case studies, we demonstrate the capability of the laboratory microCT instruments located in the Henry Moseley X-ray Imaging Facility (HMXIF) at the University of Manchester to resolve the internal micron-scale morphology of unstained rat arteries and human skin, chemically stained tendon and ligament, and *Vanessa cardui* chrysalises throughout development, as well as to visualise the 3D distribution of cells within a tissue-engineering construct. In the first case study, we illustrate that sub-micron resolutions can be achieved by imaging fixed soft tissues that have been subjected to differing loading conditions. The second case study shows that chemical staining can facilitate the differentiation between different aspects of fixed soft tissue ultrastructure and so enables quantitative measurement of fibre alignment. In the third case study, we discuss the ability of microCT to visualise living organisms through development, whereas, in the final example, we highlight the tracking of cells by osmium tetroxide staining. These case studies were selected in order to display the wide range of tissue types that can be imaged with X-ray microCT over several different length scales and by using varied techniques. They do not necessarily represent the best results that might be achieved, but are meant to give a flavour of the types of microCT methodologies that can be used for different tissue types.

### Case study 1 – arteries under pressure

As early as 1964 it was clear that the structure of large arteries is affected by internal blood pressure and that the ‘waviness’ of elastic lamellae in unpressurised vessels such as the aorta is due to the loss of luminal pressure after death (Wolinsky and Glagov, 1964). It is also recognised that the function of arteries can only be understood in the context of their 3D structure (O’Connell et al., 2008). However, over 50 years since the work of Wolinsky and Glagov on luminal pressure, arterial morphology is still routinely characterised from 2D cross-sections of unpressurised vessels. A handful of studies have attempted to characterise the internal 3D structure of the pressurised vessel wall, but the methods used, such as confocal microscopy, second-harmonic generation imaging and serial block-face electron microscopy, are all limited to the imaging of small tissue volumes and/or limited tissue components (such as fibrillar collagen) (O’Connell et al., 2008; Schrauwen et al., 2012; Schriefl et al., 2013). In our recent study, we therefore aimed to optimise and develop methods for specimen preparation, microCT imaging and image processing that would allow us to visualise, segment and measure the effects of physiological luminal pressure on the major structures of the arterial wall (Walton et al., 2015).

To that end, we dissected left and right common carotid arteries (CCA) from adult male Wistar rats and chemically fixed them at intra-luminal pressures of 0 mmHg (Fig. 2A,C) or 110 mmHg (Fig. 2B,D). Both arteries were subsequently processed by conventional histological methods (ethanol dehydration and paraffin wax embedding) before imaging on a Carl Zeiss XRM Versa-510 system (Carl Zeiss, CA, USA). By taking advantage of phase-contrast techniques and using a 20× objective, we were able to achieve a spatial resolution (in three dimensions) which approached 0.5 µm. Reconstructed arterial volumes were subsequently segmented by conventional thresholding to separate the vessel wall from the supporting paraffin and by newly developed textural separation approaches that can distinguish between ordered elastic lamellae in the medial layer and the less well-ordered collagen in the adventitia. Using these approaches, and relying on

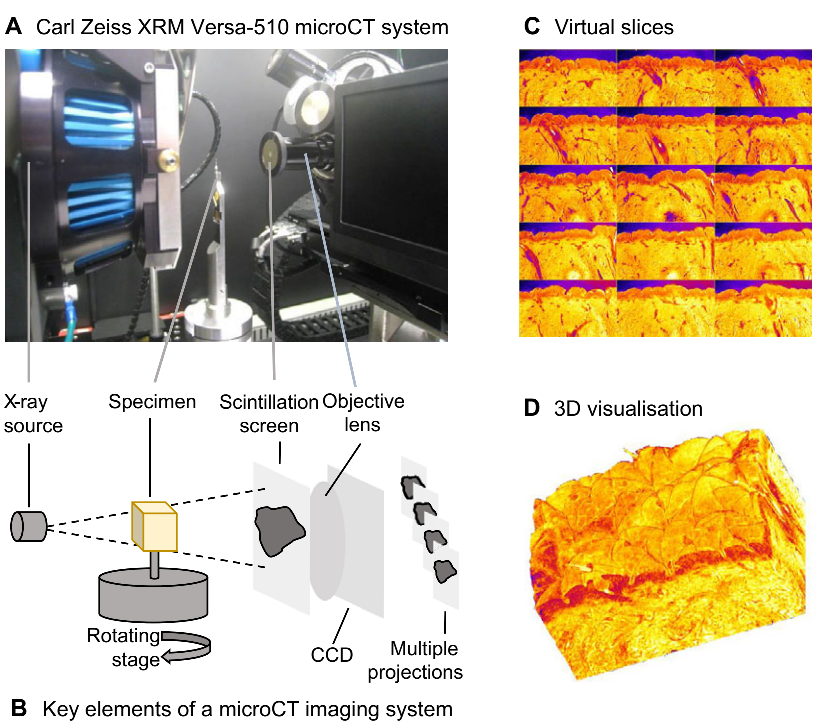


**Fig. 1. Principles of microCT.** (A,B) Interior of a Carl Zeiss microCT system with a schematic illustration of the main components: X-ray source, specimen stage and objective lenses and scintillation screens. In contrast to clinical CT, microCT instruments employ a revolving stage which rotates the specimen between an X-ray source (either laboratory or synchrotron) and a detector (usually a scintillation screen mounted in front of an objective lens) and a CCD. By collecting many projections (hundreds to thousands), virtual slices (C) and 3D visualisations (D) (in this case of human skin biopsy) can be reconstructed computationally. CCD, charge-coupled device.

microCT data alone, we were able to clearly distinguish the major components of elastic arteries, the adventitial collagen and medial elastin-rich lamellae (Fig. 2). The micro-structural detail evident in these images compares very favourably with the low contrast previously achieved in microCT cross-sections of blood vessel walls (Moritz et al., 2010).

Taken together, we were able to show that key tissue microstructures are readily identifiable in phase-contrast-enhanced X-ray tomograms of arteries and skin that have been preserved by conventional histological tissue processing methods. Discrete tissue components and regions can be segmented and hence measured by exploiting differences in X-ray absorption and morphology.

### Case study 2 – tendon and ligament fascicle alignment

Anterior cruciate ligament (ACL) rupture is one of the most severe sports-related knee injuries (Jones and Rocha, 2012). The most common treatment for a ruptured ACL is surgical reconstruction with an autografted tendon such as the patellar tendon (Mohtadi et al., 2011). Unfortunately, reconstructed knee joints often exhibit different mechanical behaviours to healthy joints; for example, in a recent study, 22 out of 26 ACL-reconstruction patients experienced differences in tibial rotation between their ACL-reconstructed and contralateral knees (Scanlan et al., 2010). One potential cause of these differences in mechanical performance could be the microstructural differences between the ACL and the graft tendons that have been used to replace it during reconstruction.

Therefore, to visualise and quantify differences in the 3D internal structure of tendons and ligaments, we used microCT to identify key geometrical differences in the arrangement of fascicles within porcine ACLs and patellar tendons that had been chemically fixed and stained with an iodine-based ($I_2KI$) X-ray contrast agent (Shearer et al., 2014). Because this microCT approach allowed us to rapidly visualise (24 min per sample) relatively large tissue volumes, the damaging consequences of mechanical sectioning were avoided.

Only patellar tendon fascicles could be stained by iodine; these were manually segmented using Avizo standard 7.0 [Visualization Sciences Group (VSG), Bordeaux, France] and individual fascicles were then tracked through the length of the tendon to determine their alignment relative to the longitudinal axis of the tendon (Fig. 3A,B). A similar technique has been used previously to track fibre bundles in human extensor carpi ulnaris tendon (Kalson et al., 2012). Although we could not directly detect individual fascicles in the ACL, there were features that could be tracked and appeared to be helically arranged (Fig. 3C,D). It is likely that these are groups of fascicles and that the gaps between individual fascicles are smaller than the voxel resolution obtained in the scans, with only the largest gaps being detectable. To measure the angle between these features

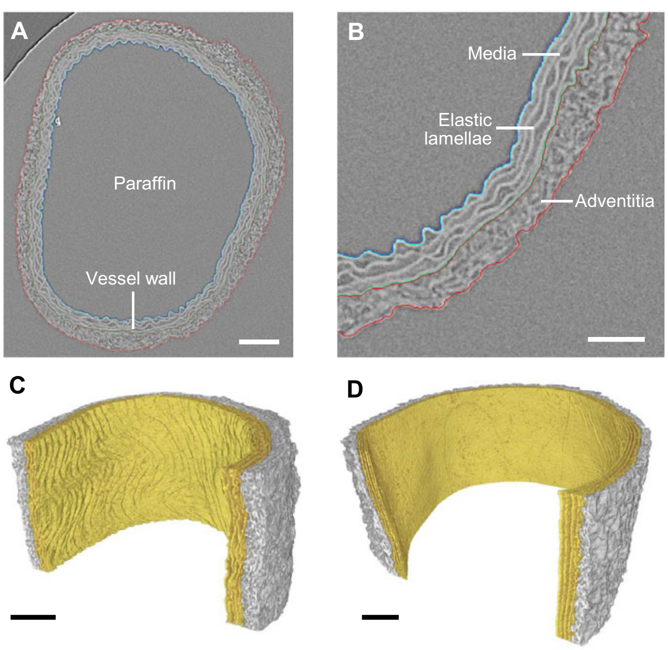


**Fig. 2. Imaging and segmentation of pressurised and unpressurised arteries.** (A) Shown here is a virtual slice extracted from an X-ray tomogram of an unpressurised rat common carotid artery. The vessel wall is more X-ray-dense than the supporting paraffin. There is no evidence of mechanical damage. Scale bar: 100 µm. (B) Segmented region from A. Boundaries between the lumen and wall (blue line), media and adventitia (green and red lines), and adventitia and external paraffin (red line) are highlighted. Scale bar: 50 µm. (C,D) 3D visualisations of unpressurised (C) and pressurised (D) rat arteries. Pressurisation reduces the thickness of both the media and adventitia, and straightens the medial elastic lamellae. Scale bars: 100 µm.

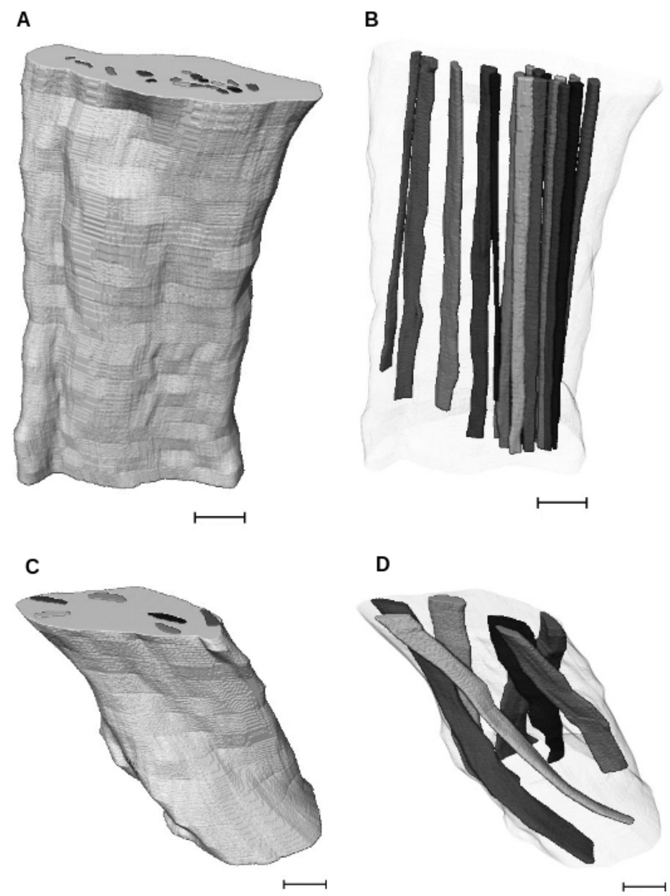


**Fig. 3. Structural differences between ligaments and tendons.** Shown here are the external surfaces (A,C) and internal 3D reconstructions (B,D) derived from microCT of $I_2KI$-stained porcine patellar tendon (A,B) and anterior cruciate ligament (ACL; C,D). The fascicles in the patellar tendon and fascicle groups in the ACL are clearly visible (B,D). The centroids of these features in each tomographic slice were tracked in MATLAB 2010a and their orientation relative to the longitudinal axis of their origin tissue was calculated. In the ACL, the features are arranged in a helix and make an angle of 24° (standard deviation 10°) with its longitudinal axis, whereas in the patellar tendon, the fascicles are much straighter and make an angle of 4° (standard deviation 2°) with its longitudinal axis. Scale bars: 2.5 mm.

and the longitudinal axis of the sample, we analysed the segmented volume files in MATLAB (MathWorks, Inc., Natick, MA, USA). The angle was found to be 4° (standard deviation of 2°) in the patellar tendon and 24° (standard deviation of 10°) in the ACL. This difference is important because the mechanical behaviour of a ligament or tendon is strongly dependent on the alignment of its fascicles (Shearer, 2015) and could go some way to explaining the differences in the stress-strain responses of the ACL and patellar tendon (Chandrashekar et al., 2008). To our knowledge, the alignment of patellar tendon and ACL fascicles has not been quantitatively measured by other techniques, such as optical or electron microscopy. Indeed, the 3D nature of fascicle alignment within a sample as large as a porcine ligament or tendon precludes the use of such techniques.

In our work, we showed that, when combined with iodine staining, microCT could effectively and non-destructively visualise 3D features within porcine ACLs and patellar tendons. Such an approach could readily be applied to image the effect of development, disease, or damage and repair in other ligaments and tendons, as well as in collagen-rich tissue-engineering constructs. Iodine-enhanced microCT has also been successfully used to visualise other soft tissue structures in a variety of samples, including, for example, embryos and insects (Metscher, 2009a,b), muscles (Jeffery et al., 2011) and cardiovascular tissues (Stephenson et al., 2012; Aslanidi et al., 2013; Butters et al., 2014).

This case study was included here because it demonstrates that microCT can be used to identify 3D substructures within a single tissue type. It also draws attention to the need to develop optimal staining methodologies. In this study, the iodine had not perfused uniformly into the centre of the samples and automatic segmentation was thus not possible. Therefore, manual segmentation had to be used, which can result in a certain degree of subjectivity owing to human error. The artefactual banding patterns, which are visible on the reconstructed sample surfaces of Fig. 3, are due to the manual segmentation of the volume at 200-slice intervals and the subsequent interpolation between segmented slices. Several factors must thus be considered when determining optimal staining techniques, including contrast agent type (as discussed below), staining times, tissue type, the fixative, temperature and pressure. Several of the studies listed above achieved sufficiently uniform iodine staining to allow automatic segmentation; however, further research is needed to determine whether the underlying techniques can be improved further. Although suboptimal staining profiles can preclude automatic segmentation, it is worth noting that local orientations in uniformly stained samples can be measured using structure tensor analysis (Varela et al., 2013), which is an automated process.

### Case study 3 – imaging of living organisms (chrysalises)

MicroCT imaging of living organisms provides information that is not available through histological methods and allows repeated scanning in the course of physiological processes such as metamorphosis in endopterygote insects (Richards et al., 2012; Lowe et al., 2013). Histology, the standard technique for studying cell morphology, is a non-quantitative, destructive procedure that requires tissue fixation and dehydration to prepare a sample for sectioning and analysis. This results in physical changes such as tissue shrinkage. In contrast, microCT of such insects not only provides data from a living and physiologically functional organism, but also enables the tracking of features within a single organism throughout its pupae development, thereby eliminating the issue of variability between different specimens and allowing four-dimensional visualisation, that is, temporal analysis of 3D structure and physiological and motor mechanisms (Lowe et al., 2013; Walker et al., 2014).

The group of Philip Withers, also at HMXIF, has demonstrated the value of microCT as a virtual histological tool for living organisms by using it to study the metamorphosis of lepidopteran pupae (Lowe et al., 2013) (Fig. 4). Throughout this *in vivo* study, *Vanessa cardui* chrysalises were imaged at varying time intervals for a total of 13 days, after which most of the butterflies hatched successfully with no apparent damage due to radiation. The scans were conducted using a Nikon Metris 225/320 kV system at 45 kV with a molybdenum target; in total, 1901 projections were taken with an exposure time of 500 ms/projection. They revealed the development of the tracheal and gut organs and, in particular, highlighted the rapid growth of the trachea, which was well-formed from the first day of pupation. The high resolution of the data allowed quantitative analysis, including the measurement of the volume of these organ systems. Interestingly, the central nervous

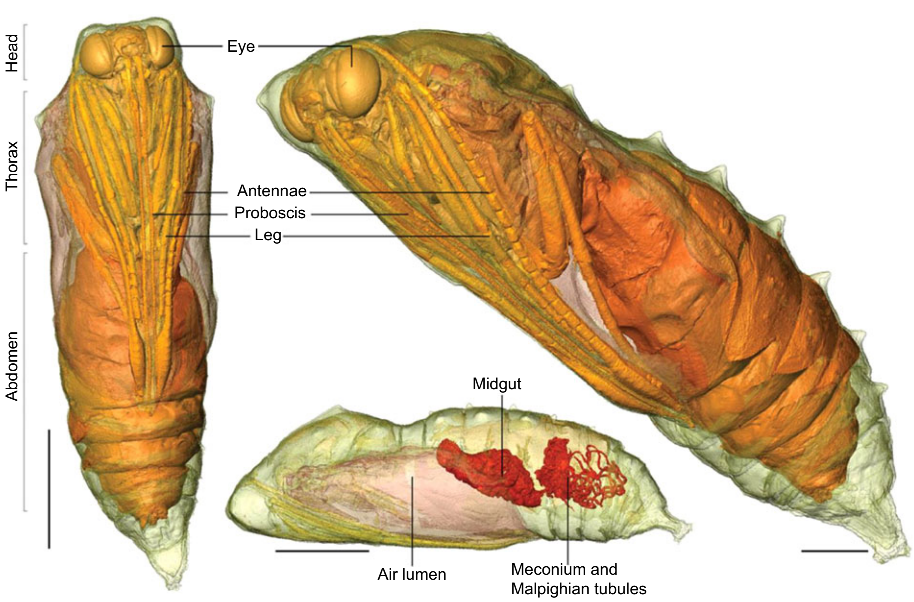


**Fig. 4. External and internal anatomy of a living chrysalis visualised by microCT.** This figure is reproduced from Lowe et al., 2013 under the Creative Commons Attribution Licence. In this article, the authors demonstrate that microCT can not only image key anatomical features in a living invertebrate but that the required X-ray exposures are compatible with normal developmental processes and subsequent hatching. The figure shows the adult at day 16 of its development; the following features of its internal and external anatomy can be seen: eyes, antennae, mouthpart, legs and gut. These features had not been visualised in 3D previously. Scale bars: 5 mm.

Journal of Cell Science (2016) 0, 1-10 doi:10.1242/jcs.179077

system and muscles could also be visualised by combining laboratory microCT with phase-contrast synchrotron imaging to avoid the use of contrast agents (Lowe et al., 2013).

Insects are ideal candidates for longitudinal microCT because of their high tolerance to radiation. For instance, Greco et al. have used microCT to study the relationship between behaviour and brain structure in *Apis mellifera* (the European honey bee) by scanning their brains and analysing their volumes (Greco et al., 2012). Although radiographic contrast agents were used, the authors were able to visualise characteristic features of the insect brain, such as optic lobes, ocelli, antennal lobes and mushroom bodies, as well as to conduct brain perfusion studies. These real-time observations of brain morphology and physiological changes have significantly contributed to the understanding of bee behaviour and brain plasticity.

### Case study 4 – visualising cell location in a tissue engineering construct

Another relevant application of microCT is the visualisation of cells to determine their location in a tissue-engineered construct, as demonstrated in the work of Dorsey et al. This team utilised osmium tetroxide staining to identify the location of cells that had been seeded onto porous polymer scaffolds for tissue engineering purposes (Dorsey et al., 2009). In this paper, the authors compared qualitative 3D microCT imaging (see Fig. 5A,C) with a commonly used alternative assessment technique, qualitative fluorescent microscopy (Fig. 5B) in combination with DNA quantification, to determine the number of cells in the construct. It was noted that, although the soluble assay gives useful information, it is limited with respect to the spatial information on the cell. Interestingly, although fluorescence imaging (Fig. 5B) resulted in higher resolution in this instance, and the soluble DNA assay was several times more sensitive than the CT imaging, microCT was able to image the entirety of the cell-seeded opaque 3D structure, and thus allowed both an image and quantitative data to be obtained in one single, non-invasive experimental technique. Based on their data, the authors suggest that this imaging technique might be used effectively for tissue-engineered constructs with a cell density of 1 million cells/ml or higher (Dorsey et al., 2009). This application is particularly important as full 3D imaging of constructs of clinical size remains a challenge in the field. Other imaging techniques only allow small portions of the constructs to be tracked, thus providing limited information at a limited scale. MicroCT, however, can be used to produce full 3D images of cell location as well as of biomaterial micro- and macro-architectural changes.

## The current state-of-the-art and future directions for microCT

### Instrumentation

Recent technological developments have focussed on improving the contrast and differentiation achieved for low-absorbing samples, as well as reducing the effects of noise on the reconstructed volumes. Advances in phase-contrast techniques are particularly promising for differentiating features within and between soft tissues. Phase-contrast techniques make use of the shift in the phase of X-rays as they propagate through a specimen, where the phase shift is determined by the 'real part' of the refractive index of the object. The real part of the refractive index for soft tissues at hard X-ray energies is typically two to three orders of magnitude greater than the imaginary part, which leads to absorption. Grating-based interferometric methods (differential phase contrast, DPC) offer high sensitivity to these phase shifts and have been transferred from the synchrotron to custom-built laboratory systems over the past 10 years (Pfeiffer et al., 2006; Bech et al., 2013; Bravin et al., 2013). Although current resolutions are limited to tens of microns, improvements in grating fabrication should see resolutions approaching 1 µm being realised. Similarly, larger area gratings are leading to the development of clinical and pre-clinical DPC systems (Stutman et al., 2011; Bravin et al., 2013; Yaroshenko et al., 2013; Scherer et al., 2014).

Advances in tomographic reconstruction algorithms (Padole et al., 2015) are enabling high-quality data to be achieved with lower doses and in shorter timescales, which is of particular importance to

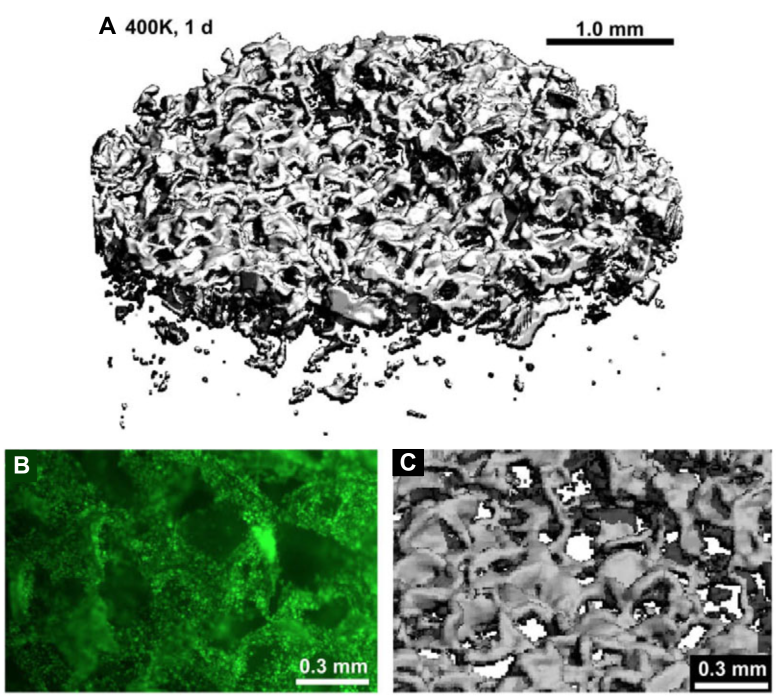


**Fig. 5. Imaging cells in a bioengineered scaffold.** (A) MicroCT image of a porous polymer scaffold cultured for 1 day with 400,000 MC3T3-E1 murine osteoblast-like cells (stained with osmium tetroxide; 1% mass fraction $OsO_4$ in PBS) and scanned using a Scanco microCT 40 with settings of 55 kV, 145 mA, 8-mm voxel size (slice thickness), 0.3 s integration, 325 slices, sigma 1.2, support 1.2 and threshold 34. Threshold 34 was used because at this value 95% of the voxels were attributable to osmium-stained cells (not scaffold or background). (B,C) Side-by-side comparison of a fluorescence micrograph (B) and a microCT image (C). Note that both images are at the exact same magnification, allowing direct structural and morphological comparison of the fluorescence and microCT images detailing live-cell location and mineralized matrix production, respectively. The green dots in (B) are fluorescently stained nuclei of cells adhered to scaffolds. The grey contours in C represent confluent cell layers (not scaffold). Figure reproduced from Dorsey et al., 2009 with kind permission of Elsevier.

microCT studies of dynamically changing living tissues. State-of-the-art algorithms include for example ADS-POCS [with total variation regularisation (Han et al., 2011)] and the equally sloped acquisition and reconstruction scheme (Fahimian et al., 2010).

Another major technological advance on the horizon is spectral CT, which has the potential to lead to a step change in characterising both tissue structure (as a consequence of enhanced contrast) and composition. Specifically, spectral CT utilises energy-sensitive detectors to measure incident X-ray photon energy in addition to the X-ray intensity as recorded by conventional detectors. These detectors either determine the energy to within a number of broad bands (bins), such as the Medipix detector (He et al., 2013), or offer much finer sampling of the energy spectrum, such as the HEXITEK hyperspectral imaging detector (Jacques et al., 2013). With spectral CT, a defined energy range can be selected for tomographic reconstruction, which allows the contrast between tissues to be optimised while reducing or eliminating beam-hardening artefacts. Furthermore, the elemental or material composition of the tissue can be deduced. This technique will be particularly powerful when used in combination with contrast agents, as it offers selective molecular imaging and the ability to differentiate between multiple contrast agents applied to the same tissue (Schirra et al., 2014). For further details regarding recent developments in microCT, the reader is referred to a recent review (Ritman, 2011).

### Specimen preparation and labelling

In order to enhance contrast or track particular features in a sample, specimens are often either chemically stained or labelled by particle tagging. Chemical staining, that is, immersing the sample in a contrast agent, is a simple process that has proven to be effective for a wide range of samples (Metscher, 2009a,b). An ideal contrast agent should perfuse rapidly and uniformly into the centre of a sample without deforming it, and should preferably be non-toxic. The stain should bind to a particular feature of interest and have a substantially higher density than the tissue it is staining in order to increase the attenuation of X-rays, and therefore the contrast, between different tissue types in the sample. To date, certain contrast agents (such as iodine and phosphotungstic acid, for example) have been widely used because they meet several of the criteria above. However, these contrast agents are not perfect; iodine is known to cause substantial sample shrinkage (Vickerton et al., 2013) and phosphotungstic acid perfusion can take a long time, making it unsuitable for larger samples (Shearer et al., 2014).

One current area of interest is to identify the most effective contrast agents for different types of sample. For example, Pauwels et al. compared the ability of 28 distinct chemicals to enhance contrast in porcine adipose and muscle tissue, as well as in mouse legs, and found that phosphotungstic acid, phosphomolybdic acid and ammonium orthomolybdate result in the best contrast between tissue types, whereas potassium iodide and sodium tungstate appear to penetrate large samples most effectively (Pauwels et al., 2013). Another recent study investigated the effects of using different fixatives on contrast and found Bouin's solution to be superior to 70% ethanol and 2.5% glutaraldehyde (Sombke et al., 2015). As an alternative to chemical staining, critical point drying has recently been used (Zysk et al., 2012; Sombke et al., 2015) to enhance endogenous (absorption and phase) contrast by removing water, which has a similar refractive index coefficient to many soft tissue components. A key strength of optical microscopy is the ability to identify specific tissue components immunohistochemically, and indeed, recently, a promising metal-based immuno-detection technique has been described that enables the localisation of specific molecular epitopes by microCT (Metscher and Müller, 2011). This technique uses standard enzyme-conjugated secondary antibodies with a substituted metal deposition scheme of an 'enzyme metallography' kit (Nanoprobes EnzMet 6010) for the usual chromogen reactions. Using this approach, microCT visualisations of acetylated α-tubulin in the chick nervous system and of type II collagen in developing limbs could be obtained (Metscher and Müller, 2011).

Particle tagging can also be used to enhance contrast or to track features of interest in microCT. A current research goal is to determine effective particle compositions for microCT contrast agents to label and visualise live cells; so far, gold and bismuth nanoparticles have been used successfully (Naha et al., 2014; Swy et al., 2014; Zhu et al., 2014). These studies demonstrate that 40-nm bismuth particle cores encapsulated in 120-nm poly(lactic-*co*-glycolic acid) (PLGA) are biocompatible and able to offer economical advantage over gold, which is 1000 times more expensive than bismuth. These heavy metal particles can be tagged to specific attachment sites on living cells. For example, polyethylene glycolated folic acid modification of multifunctional dendrimer-entrapped gold nanoparticles enables efficient targeting of the particles to cancer cells that overexpress folic acid receptors. These labelled cells can then be imaged *in vitro*, or *in vivo* in a xenografted tumor model (Zhu et al., 2014). Furthermore, superparamagnetic iron oxide nanoparticles have also been used to track cells that have been implanted in tissue-engineered grafts in pre-clinical models with microCT or MRI (Mertens et al., 2014; Pacak et al., 2014).

### Imaging of dynamic processes

The 3D structure of a biological system might change either rapidly, as a consequence of movement, or more slowly due to growth, ageing and disease. MicroCT can be utilised in both scenarios. For example, flight in small insects such as the blowfly *Calliphora vicina* is dependent on reversible rearrangements in the internal power muscles, which deform the thorax and hence oscillate the wings. In their recent study, Walker and colleagues used the TOMCAT beamline at the Swiss Light Source (Stampanoni et al., 2010) in combination with stereo high-speed photogrammetry to visualise the repetitive movement of muscles and tendons of a living fly at sub-millisecond timescales and micron-scale spatial resolutions (Walker et al., 2014). Non-repetitive movements over longer timescales can also be visualised by microCT alone. Developmental biological processes, for example, typically induce irreversible changes in 3D structure of tissues over days or months and, in cases such as that described in case study 3, can be visualised by performing sequential scans. These recent studies (Richards et al., 2012; Lowe et al., 2013; Walker et al., 2014) demonstrate that it is already possible to visualise dynamic changes in a living biological system with microCT. Nevertheless, there is considerable scope for continued instrumental development in order to improve contrast, whereas the need to exercise caution with regards to the impact of X-ray exposure on the welfare and biological function of living organisms should not be overlooked.

## Concluding remarks

In this Commentary, we have discussed the ability of microCT to image a variety of biological samples. Four case studies have been presented as examples. The first two demonstrated the potential of microCT to resolve fibre bundle orientation within soft tissues in 3D, which is only possible using conventional histology in combination with laborious, error-prone and potentially artefactinducing (as a consequence of residual strain release) serial sectioning. The third case study showed that microCT can be used to image living organisms throughout development, which cannot be done using techniques that require samples to be fixed and/or dissected. Modifications to the standard microCT protocol, such as staining and phase contrast, have allowed the imaging of soft materials in tissue-engineered constructs, allowing a complete follow-up of cell location, migration and even organ growth over a period of time. This application continues to be developed as teams focus on non-destructive strategies to image clinical constructs in 3D. Finally, the fourth case study demonstrated how CT imaging can be used in conjunction with traditional fluorescent microscopy to create a synergistic data set relating to cell viability, location and extracellular matrix production not just in qualitative spatial terms but also local quantitative volumes to give guidance on the choice of correct tissue culture protocols. In summary, we believe that the potential of microCT has not yet been fully realised in the biological science community. The ability of this X-ray-based approach to rapidly image relatively large tissue volumes at high resolution could be harnessed both as a stand-alone technique and in combination with other methodologies.

#### Acknowledgements
The authors would like to acknowledge the assistance provided by the Manchester X-ray Imaging Facility (which was funded in part by the Engineering and Physical Sciences Research Council (ESPRC) [grant numbers EP/F007906/1, EP/F001452/1 and EP/I02249X/1]) and the expert advice of Peter March and Tobias Starborg of the University of Manchester Faculty of Lifesciences Bioimaging and Electron Microscopy Core Facilities. The skin microCT data presented in Fig. 1 was obtained by Mr Chris Keeble whose studentship was funded by Walgreens Boots Alliance (award to M.J.S.). This is a review article, and therefore all data underlying this study is cited in the references.

#### Competing interests
The authors declare no competing or financial interests.

#### Author contributions
All authors contributed to the writing and approval of the manuscript.

#### Funding
T.S. would like to thank the Engineering and Physical Sciences Research Council (EPSRC) for funding his work through fellowship grants [grant number EP/L017997/1]; M.J.S. would like to acknowledge funding by the Medical Research Council [grant number G1001398].

#### References
**Abbott, E. A.** (2010). *Flatland: An Edition with Notes and Commentary/Edwin A. Abbott an Edition with Notes and Commentary by William F. Lindgren, Thomas F. Banchoff*. Cambridge: Cambridge University Press.

**Aslanidi, O. V., Nikolaidou, T., Jichao Zhao, T., Smaill, B. H., Gilbert, S. H., Holden, A. V., Lowe, T., Withers, P. J., Stephenson, R. S., Jarvis, J. C. et al.** (2013). Application of micro-computed tomography with iodine staining to cardiac imaging, segmentation, and computational model development. *IEEE Trans. Med. Imaging* **32**, 8-17.

**Badea, A. and Johnson, A.** (2013). Magnetic resonance microscopy. In *Biophotonics in Pathology* (ed. S. Cohen), pp. 153-184. IOS Press.

**Balint, R., Lowe, T. and Shearer, T.** (2016). Optimal contrast agent staining of ligament and tendons for X-ray computed tomography. *PLoS ONE* **11**, e0153552.

**Bech, M., Tapfer, A., Velroyen, A., Yaroshenko, A., Pauwels, B., Hostens, J., Bruyndonckx, P., Sasov, A. and Pfeiffer, F.** (2013). *In-vivo* dark-field and phase-contrast x-ray imaging. *Sci. Rep.* **3**, 3209.

**Bravin, A., Coan, P. and Suortti, P.** (2013). X-ray phase-contrast imaging: from pre-clinical applications towards clinics. *Phys. Med. Biol.* **58**, R1-R35.

**Burton, R. A. B., Lee, P., Casero, R., Garny, A., Siedlecka, U., Schneider, J. E., Kohl, P. and Grau, V.** (2014). Three-dimensional histology: tools and application to quantitative assessment of cell-type distribution in rabbit heart. *Europace* **16**, iv86-iv95.

**Butters, T. D., Castro, S. J., Lowe, T., Zhang, Y., Lei, M., Withers, P. J. and Zhang, H.** (2014). Optimal iodine staining of cardiac tissue for X-ray computed tomography. *PLoS ONE* **9**, e105552.

**Canty, E. G., Starborg, T., Lu, Y., Humphries, S. M., Holmes, D. F., Meadows, R. S., Huffman, A., O'Toole, E. T. and Kadler, K. E.** (2006). Actin filaments are required for fibripositor-mediated collagen fibril alignment in tendon. *J. Biol. Chem.* **281**, 38592-38598.

**Cartmell, S., Huynh, K., Lin, A., Nagaraja, S. and Guldberg, R.** (2004). Quantitative microcomputed tomography analysis of mineralization within three-dimensional scaffolds in vitro. *J. Biomed. Mater. Res. A* **69A**, 97-104.

**Cartmell, S. H., Thurstan, S. P., Gittings, J. P., Griffiths, S., Bowen, C. R. and Turner, I. G.** (2014). Polarization of porous hydroxyapatite scaffolds: influence on osteoblast cell proliferation and extracellular matrix production. *J. Biomed. Mater. Res. A* **102**, 1047-1052.

**Chandrashekar, N., Hashemi, J., Slauterbeck, J. and Beynnon, B. D.** (2008). Low-load behaviour of the patellar tendon graft and its relevance to the biomechanics of the reconstructed knee. *Clin. Biomech.* **23**, 918-925.

**Cox, G., Kable, E., Jones, A., Fraser, I., Manconi, F. and Gorrell, M. D.** (2003). 3-dimensional imaging of collagen using second harmonic generation. *J. Struct. Biol.* **141**, 53-62.

**Craig, J. W.** (1936). "Tomography" Report on a Method of X-raying sections of the body. *British Journal of Tuberculosis* **30**, 152-154.

**Dorsey, S. M., Lin-Gibson, S. and Simon, C. G., Jr.** (2009). X-ray microcomputed tomography for the measurement of cell adhesion and proliferation in polymer scaffolds. *Biomaterials* **30**, 2967-2974.

**Elliott, J. C. and Dover, S. D.** (1982). X-ray microtomography. *J. Microsc.* **126**, 211-213.

**Elliott, J. C., Dowker, S. E. P. and Knight, R. D.** (1981). Scanning X-ray microradiography of a section of a carious lesion in dental enamel. *J. Microsc.* **123**, 89-92.

**Fahimian, B. P., Mao, Y., Cloetens, P. and Miao, J.** (2010). Low-dose x-ray phase-contrast and absorption CT using equally sloped tomography. *Phys. Med. Biol.* **55**, 5383-5400.

**Folch, A., Mezzour, S., Düring, M., Hurtado, O., Toner, M. and Müller, R.** (2000). Stacks of microfabricated structures as scaffolds for cell culture and tissue engineering. *Biomed. Microdevices* **2**, 207-214.

**Geyer, S. H., Tinhofer, I. E., Lumenta, D. B., Kamolz, L.-P., Branski, L., Finnerty, C. C., Herndon, D. N. and Weninger, W. J.** (2015). High-resolution episcopic microscopy (HREM): A useful technique for research in wound care. *Ann. Anat.* **197**, 3-10.

**Greco, M. K., Tong, J., Soleimani, M., Bell, D. and Schäfer, M. O.** (2012). Imaging live bee brains using minimally-invasive diagnostic radioentomology. *J. Insect Sci.* **12**, 89.

**Han, X., Bian, J., Eaker, D. R., Kline, T. L., Sidky, E. Y., Ritman, E. L. and Pan, X.** (2011). Algorithm-enabled low-dose micro-CT imaging. *IEEE Trans. Med. Imaging* **30**, 606-620.

**He, P., Yu, H., Bennett, J., Ronaldson, P., Zainon, R., Butler, A., Butler, P., Wei, B. and Wang, G.** (2013). Energy-discriminative performance of a spectral micro-CT system. *J. X-Ray Sci. Technol.* **21**, 335-345.

**Hildebrand, T. and Rüegsegger, P.** (1997). A new method for the model-independent assessment of thickness in three-dimensional images. *J. Microsc.* **185**, 67-75.

**Hvid, I., Bentzen, S. M., Linde, F., Mosekilde, L. and Pongsoipetch, B.** (1989). X-ray quantitative computed tomography: the relations to physical properties of proximal tibial trabecular bone specimens. *J. Biomech.* **22**, 837-844.

**Jacques, S. D. M., Egan, C. K., Wilson, M. D., Veale, M. C., Seller, P. and Cernik, R. J.** (2013). A laboratory system for element specific hyperspectral X-ray imaging. *Analyst* **138**, 755-759.

**Jeffery, N. S., Stephenson, R. S., Gallagher, J. A., Jarvis, J. C. and Cox, P. G.** (2011). Micro-computed tomography with iodine staining resolves the arrangement of muscle fibres. *J. Biomech.* **44**, 189-192.

**Jones, H. and Rocha, P. C.** (2012). Prevention in ACL injuries. In *Sports Injuries* (ed. M. N. Doral), pp. 33-42. Berlin; Heidelberg: Springer-Verlag.

**Kalson, N. S., Malone, P. S. C., Bradley, R. S., Withers, P. J. and Lees, V. C.** (2012). Fibre bundles in the human extensor carpi ulnaris tendon are arranged in a spiral. *J. Hand Surg.* **37**, 550-554.

**Keyes, S. D., Boardman, R. P., Marchant, A., Roose, T. and Sinclair, I.** (2013). A robust approach for determination of the macro-porous volume fraction of soils with X-ray computed tomography and an image processing protocol. *Eur. J. Soil Sci.* **64**, 298-307.

**Lowe, T., Garwood, R. J., Simonsen, T. J., Bradley, R. S. and Withers, P. J.** (2013). Metamorphosis revealed: time-lapse three-dimensional imaging inside a living chrysalis. *J. R. Soc. Interface* **10**, 20130304.

**Maire, E. and Withers, P. J.** (2014). Quantitative X-ray tomography. *Int. Mater. Rev.* **59**, 1-43.

**Mertens, M. E., Frese, J., Bölükbas, D. A., Hrdlicka, L., Golombek, S., Koch, S., Mela, P., Jockenhövel, S., Kiessling, F. and Lammers, T.** (2014). FMN-coated fluorescent USPIO for cell labeling and non-invasive MR imaging in tissue engineering. *Theranostics* **4**, 1002-1013.

**Metscher, B. D.** (2009a). MicroCT for developmental biology: a versatile tool for high-contrast 3D imaging at histological resolutions. *Dev. Dyn.* **238**, 632-640.

**Metscher, B. D.** (2009b). MicroCT for comparative morphology: simple staining methods allow high-contrast 3D imaging of diverse non-mineralized animal tissues. *BMC Physiol.* **9**, 11.

**Metscher, B. D. and Müller, G. B.** (2011). MicroCT for molecular imaging: quantitative visualization of complete three-dimensional distributions of gene products in embryonic limbs. *Dev. Dyn.* **240**, 2301-2308.

**Mohtadi, N. G. H., Chan, D. S., Dainty, K. N. and Whelan, D. B.** (2011). Patellar tendon versus hamstring tendon autograft for anterior cruciate ligament rupture in adults (review). *Cochrane Libr.*, CD005960.

**Moritz, R., Eaker, D. R., Langheinrich, A. C., Jorgensen, S. M., Bohle, R. M. and Ritman, E. L.** (2010). Quantification of vasa vasorum density in multi-slice computed tomographic coronary angiograms: role of computed tomographic image voxel size. *J. Comput. Assist. Tomogr.* **34**, 273-278.

**Müller, R., Hildebrand, T. and Ruegsegger, P.** (1994). Non-invasive bone biopsy: A new method to analyse and display the three-dimensional structure of trabecular bone. *Phys. Med. Biol.* **39**, 145-164.

**Müller, R., Hildebrand, T. and Rüegsegger, P.** (1997). Structural properties of trabecular bone from different sites of the human skeleton: a descriptive study. *Trans. Eur. Orthop. Res. Soc.* **7**, 275.

**Naha, P. C., Al Zaki, A., Hecht, E., Chorny, M., Chhour, P., Blankemeyer, E., Yates, D. M., Witschey, W. R. T., Litt, H. I., Tsourkas, A. et al.** (2014). Dextran coated bismuth–iron oxide nanohybrid contrast agents for computed tomography and magnetic resonance imaging. *J. Mater. Chem. B* **2**, 8239-8248.

**Nakayama, H., Burns, D. M. and Kawase, T.** (2011). Nondestructive microstructural analysis of porous bioceramics by microfocus X-ray computed tomography (μCT): a proposed protocol for standardized evaluation of porosity and interconnectivity between macro-pores. *J. Nondestruct. Eval.* **30**, 71-80.

**Navarro, F. A., So, P. T. C., Nirmalan, R., Kropf, N., Sakaguchi, F., Park, C. S., Lee, H. B. and Orgill, D. P.** (2004). Two-photon confocal microscopy: a nondestructive method for studying wound healing. *Plast. Reconstr. Surg.* **114**, 121-128.

**Norton, C. L.** (1896). The X-rays in medicine and surgery. *Science* **3**, 730-731.

**O'Connell M. K., Murthy S., Phan S., Xu C., Buchanan J., Spilker R., Dalman R. L., Zarins C. K., Denk W. and Taylor C. A.** (2008). The three-dimensional micro- and nanostructure of the aortic medial lamellar unit measured using 3D confocal and electron microscopy imaging. *Matrix Biol.* **27**, 171-181.

**Pacak, C. A., Hammer, P. E., MacKay, A. A., Dowd, R. P., Wang, K.-R., Masuzawa, A., Sill, B., McCully, J. D. and Cowan, D. B.** (2014). Superparamagnetic iron oxide nanoparticles function as a long-term, multi-modal imaging label for non-invasive tracking of implanted progenitor cells. *PLoS ONE* **9**, e108695.

**Padole, A., Khawaja, R. D. A., Kalra, M. K. and Singh, A.** (2015). CT radiation dose and iterative reconstruction techniques. *Am. J. Roentgenol.* **204**, W384-W392.

**Pauwels, E., Van Loo, D., Cornillie, P., Brabant, L. and Van Hoorebeke, L.** (2013). An exploratory study of contrast agents for soft tissue visualization by means of high resolution X-ray computed tomography imaging. *J. Microsc.* **250**, 21-31.

**Peddie, C. J. and Collinson, L. M.** (2014). Exploring the third dimension: volume electron microscopy comes of age. *Micron* **61**, 9-19.

**Pfeiffer, F., Weitkamp, T., Bunk, O. and David, C.** (2006). Phase retrieval and differential phase-contrast imaging with low-brilliance X-ray sources. *Nat. Phys.* **2**, 258-261.

**Popp, A. W., Windolf, M., Senn, C., Tami, A., Richards, R. G., Brianza, S. and Schiuma, D.** (2012). Prediction of bone strength at the distal tibia by HR-pQCT and DXA. *Bone* **50**, 296-300.

**Rastogi, V., Puri, N., Arora, S., Kaur, G., Yadav, L. and Sharma, R.** (2013). Artefacts: a diagnostic dilemma – a review. *J. Clin. Diagn. Res.* **7**, 2408-2413.

**Richards, C. S., Simonsen, T. J., Abel, R. L., Hall, M. J. R., Schwyn, D. A. and Wicklein, M.** (2012). Virtual forensic entomology: improving estimates of minimum post-mortem interval with 3D micro-computed tomography. *Forensic Sci. Int.* **220**, 251-264.

**Ritman, E. L.** (2011). Current status of developments and applications of micro-CT. *Annu. Rev. Biomed. Eng.* **13**, 531-552.

**Röntgen, W. C.** (1895). Über eine neue Art von Strahlen. *Sitzung* **30**, 132-141.

**Rüegsegger, P., Koller, B. and Müller, R.** (1996). A microtomographic system for the nondestructive evaluation of bone architecture. *Calcif. Tissue Int.* **58**, 24-29.

**Scanlan, S. F., Chaudhari, A. M. W., Dyrby, C. O. and Andriacchi, T. P.** (2010). Differences in tibial rotation during walking in ACL reconstructed and healthy contralateral knees. *J. Biomech.* **43**, 1817-1822.

**Scherer, K., Birnbacher, L., Chabior, M., Herzen, J., Mayr, D., Grandl, S., Sztrókay-Gaul, A., Hellerhoff, K., Bamberg, F. and Pfeiffer, F.** (2014). Bi-directional X-ray phase-contrast mammography. *PLoS ONE* **9**, e93502.

**Schirra, C. O., Brendel, B., Anastasio, M. A. and Roessl, E.** (2014). Spectral CT: a technology primer for contrast agent development. *Contrast Media Mol. Imaging* **9**, 62-70.

**Schmitt, O., Modersitzki, J., Heldmann, S., Wirtz, S. and Fischer, B.** (2007). Image registration of sectioned brains. *Int. J. Comput. Vis.* **73**, 5-39.

**Schrauwen, J. T. C., Vilanova, A., Rezakhaniha, R., Stergiopulos, N., van de Vosse, F. N. and Bovendeerd, P. H. M.** (2012). A method for the quantification of the pressure dependent 3D collagen configuration in the arterial adventitia. *J. Struct. Biol.* **180**, 335-342.

**Schriefl, A. J., Wolinski, H., Regitnig, P., Kohlwein, S. D. and Holzapfel, G. A.** (2013). An automated approach for three-dimensional quantification of fibrillar structures in optically cleared soft biological tissues. *J. R. Soc. Interface* **10**, 20120760.

**Shapiro, E. M., Skrtic, S., Sharer, K., Hill, J. M., Dunbar, C. E. and Koretsky, A. P.** (2004). MRI detection of single particles for cellular imaging. *Proc. Natl. Acad. Sci. USA* **101**, 10901-10906.

**Sharpe, J., Ahlgren, U., Perry, P., Hill, B., Ross, A., Hecksher-Sørensen, J., Bladock, R. and Davidson, D.** (2002). Optical projection tomography as a tool for 3D microscopy and gene expression studies. *Science* **296**, 541-545.

**Shearer, T.** (2015). A new strain energy function for modelling ligaments and tendons whose fascicles have a helical arrangement of fibrils. *J. Biomech.* **48**, 3017-3025.

**Shearer, T., Rawson, S., Castro, S. J., Balint, R., Bradley, R. S., Lowe, T., Vila-Comamala, J., Lee, P. D. and Cartmell, S. H.** (2014). X-ray computed tomography of the anterior cruciate ligament and patellar tendon. *Muscles Ligaments Tendons J.* **4**, 238-244.

**Sombke, A., Lipke, E., Michalik, P., Uhl, G. and Harzsch, S.** (2015). Potential and limitations of X-ray micro-computed tomography in arthropod neuroanatomy: a methodological and comparative survey. *J. Comp. Neurol.* **523**, 1281-1295.

**Stampanoni, M., Marone, F., Modregger, P., Pinzer, B., Thuring, T., Vila-Comamala, J., David, C. and Mokso, R.** (2010). Tomographic hard X-ray phase contrast micro- and nano-imaging at TOMCAT. In *6th International Conference on Medical Applications of Synchrotron Radiation*, Vol. 1266 (ed. K. K. W. Siu), pp. 13-17. Melville: Amer Inst Physics.

**Stephenson, R. S., Boyett, M. R., Hart, G., Nikolaidou, T., Cai, X., Corno, A. F., Alphonso, N., Jeffery, N. and Jarvis, J. C.** (2012). Contrast enhanced micro-computed tomography resolves the 3-dimensional morphology of the cardiac conduction system in mammalian hearts. *PLoS ONE* **7**, e35299.

**Stock, S. R.** (2008). Recent advances in X-ray microtomography applied to materials. *Int. Mater. Rev.* **53**, 129-181.

**Stutman, D., Beck, T. J., Carrino, J. A. and Bingham, C. O.** (2011). Talbot phase-contrast x-ray imaging for the small joints of the hand. *Phys. Med. Biol.* **56**, 5697-5720.

**Swy, E. R., Schwartz-Duval, A. S., Shuboni, D. D., Latourette, M. T., Mallet, C. L., Parys, M., Cormode, D. P. and Shapiro, E. M.** (2014). Dual-modality, fluorescent, PLGA encapsulated bismuth nanoparticles for molecular and cellular fluorescence imaging and computed tomography. *Nanoscale* **6**, 13104-13112.

**Tapia, J. C., Kasthuri, N., Hayworth, K. J., Schalek, R., Lichtman, J. W., Smith, S. J. and Buchanan, J.** (2012). High-contrast en bloc staining of neuronal tissue for field emission scanning electron microscopy. *Nat. Protoc.* **7**, 193-206.

**Thyng, F. W.** (1914). The anatomy of a 17.8 mm. human embryo. *Am. J. Anat.* **17**, 31-112.

**Varela, M., Zhao, J. and Aslanidi, O. V.** (2013). Determination of atrial orientation using structure tensor analysis for biophysical modelling. In *Functional Imaging and Modeling of the Heart* (ed. S. Ourselin, D. Rueckert and N. Smith), pp. 425-432. Springer.

**Vickerton, P., Jarvis, J. and Jeffery, N.** (2013). Concentration-dependent specimen shrinkage in iodine-enhanced microCT. *J. Anat.* **223**, 185-193.

**Walker, S. M., Schwyn, D. A., Mokso, R., Wicklein, M., Müller, T., Doube, M., Stampanoni, M., Krapp, H. G. and Taylor, G. K.** (2014). In vivo time-resolved microtomography reveals the mechanics of the blowfly flight motor. *PLoS Biol.* **12**, e1001823.

**Walton, L. A., Bradley, R. S., Withers, P. J., Newton, V. L., Watson, R. E. B., Austin, C. and Sherratt, M. J.** (2015). Morphological characterisation of unstained and intact tissue micro-architecture by X-ray computed micro- and nano-tomography. *Sci. Rep.* **5**, 10074.

**Weninger, W. J., Meng, S., Streicher, J. and Müller, G. B.** (1998). A new episcopic method for rapid 3-D reconstruction: applications in anatomy and embryology. *Anat. Embryol.* **197**, 341-348.

**Withers, P. J.** (2007). X-ray nanotomography. *Mater. Today* **10**, 26-34.

**Wolinsky, H. and Glagov, S.** (1964). Structural basis for the static mechanical properties of the aortic media. *Circ. Res.* **14**, 400-413.

**Yang, Z., Berr, S. S., Gilson, W. D., Toufektsian, M.-C. and French, B. A.** (2004). Simultaneous evaluation of infarct size and cardiac function in intact mice by contrast-enhanced cardiac magnetic resonance imaging reveals contractile dysfunction in noninfarcted regions early after myocardial infarction. *Circulation* **109**, 1161-1167.

**Yaroshenko, A., Meinel, F. G., Bech, M., Tapfer, A., Velroyen, A., Schleede, S., Auweter, S., Bohla, A., Yildirim, A. Ö., Nikolaou, K. et al.** (2013). Pulmonary emphysema diagnosis with a preclinical small-animal X-ray dark-field scatter-contrast scanner. *Radiology* **269**, 427-433.

**Zankel, A., Kraus, B., Poelt, P., Schaffer, M. and Ingolic, E.** (2009). Ultramicrotomy in the ESEM, a versatile method for materials and life sciences. *J. Microsc.* **233**, 140-148.

**Zhu, J., Zheng, L., Wen, S., Tang, Y., Shen, M., Zhang, G. and Shi, X.** (2014). Targeted cancer theranostics using alpha-tocopheryl succinate-conjugated multifunctional dendrimer-entrapped gold nanoparticles. *Biomaterials* **35**, 7635-7646.

**Zysk, A. M., Garson, A. B., III, Xu, Q., Brey, E. M., Zhou, W., Brankov, J. G., Wernick, M. N., Kuszak, J. R. and Anastasio, M. A.** (2012). Nondestructive volumetric imaging of tissue microstructure with benchtop x-ray phase-contrast tomography and critical point drying. *Biomed. Opt. Expr.* **3**, 1924-1932.